

Estimating geomechanical parameters from microseismic plane focal mechanisms recorded during multistage hydraulic fracturing

Wenhuan Kuang¹, Mark Zoback², and Jie Zhang³

ABSTRACT

We extend a full-waveform modeling method to invert source focal-plane mechanisms for microseismic data recorded with dual-borehole seismic arrays. Combining inverted focal-plane mechanisms with geomechanics knowledge, we map the pore pressure distribution in the reservoir. Determining focal mechanisms for microseismic events is challenging due to poor geometry coverage. We use the P-wave polarities, the P- and S-wave similarities, the SV/P amplitude ratio, and the SH/P amplitude ratio to invert the focal-plane mechanisms. A synthetic study proves that this method can effectively resolve focal mechanisms with dual-array geometry. We apply this method to 47 relatively

large events recorded during a hydraulic fracturing operation in the Barnett Shale. The focal mechanisms are used to invert for the orientation and relative magnitudes of the principal stress axes, the orientation of the planes slipping in shear, and the approximate pore pressure perturbation that caused the slip. The analysis of the focal mechanisms consistently shows a normal faulting stress state with the maximum principal stress near vertical, the maximum horizontal stress near horizontal at an azimuth of N60°E, and the minimum horizontal stress near horizontal at an azimuth of S30°E. We propose a general method that can be used to obtain microseismic focal-plane mechanisms and use them to improve the geomechanical understanding of the stimulation process during multistage hydraulic fracturing.

INTRODUCTION

Over the past 10 years, it has been widely demonstrated that production from unconventional gas and oil reservoirs can be stimulated by multistage hydraulic fracturing in horizontal wells. During stimulation, opening-mode hydraulic fractures are formed and propagate away from the wellbores at an orientation perpendicular to the least principal stress, and shear slip is activated on preexisting faults, which induce multiple microseismic events (Warpinski, 2009; Warpinski and Du, 2010; Warpinski et al., 2012; Li et al., 2014; Song et al., 2014). Many recent studies investigate the reactivation of faults in hydraulic fracturing, which triggers repeated events with an almost-identical waveform signature. For instance, Li et al. (2014) find that some of the largest events in a hydraulic treatment have almost identical waveforms, likely from a repeatedly reactivated fault nearby. This process typically creates microseismic events with magnitudes ranging from -3 to -1 (Duncan, 2005). The combination of

hydraulic fracturing and shear slip on a preexisting fault (as evidenced by the microseismicity) can increase the effective permeability thus enhancing the production. Microseismic locations have been studied and widely used to characterize the stimulation process, including fracture azimuth, length, height growth, complexity, diversion, zonal coverage, stimulated reservoir volume, and fault interactions (Warpinski et al., 2012). In this study, we attempt to derive important geomechanical parameters from microseismic focal-plane mechanisms to provide more information about the activated fractures, local stress field, fracture geometry, and pore pressure perturbation that causes the slip so that we can better understand and optimize the reservoir stimulation.

Estimating the source focal mechanism is an important task in earthquake seismology, and many efforts have been made to improve accuracy and efficiency. Guilhem and Dreger (2011) perform linear moment-tensor inversion over a set of grids with precalculated Green's functions. Tsuruoka et al. (2009) solve a waveform

Manuscript received by the Editor 16 December 2015; revised manuscript received 14 July 2016; published online 11 November 2016.

¹Formerly Stanford University, Department of Geophysics, Stanford, California, USA; presently University of Science and Technology of China, Geophysical Research Institute, Hefei, China. E-mail: kuangwh@mail.ustc.edu.cn.

²Stanford University, Department of Geophysics, Stanford, California, USA. E-mail: zoback@stanford.edu.

³University of Science and Technology of China, Geophysical Research Institute, Hefei, China. E-mail: jzhang25@ustc.edu.cn.

© 2017 Society of Exploration Geophysicists. All rights reserved.

grid-search problem with long-period data. Zhang et al. (2014) develop an efficient search engine method to determine the source locations and the source focal mechanisms with long-period data recorded at three or more seismic stations. However, determining focal mechanisms for microseismic events induced during hydraulic fracturing can be challenging due to the limited geometry coverage, particularly compared with seismometers that record earthquakes from locations all over the world. In general, downhole monitoring arrays provide small angular coverage of the seismic radiation from the event. As a result, it is challenging, if not impossible, to use only P-wave polarities to constrain focal mechanisms as in conventional methods. Therefore, additional waveform information (such as S/P ratios) is needed to better constrain microseismic focal mechanisms (Warpinski and Du, 2010; Staněk et al., 2014). Many authors address the uncertainties of focal mechanism inversion for microseismic events (Warpinski and Du, 2010; Song et al., 2014; Witten and Shragge, 2015). Li et al. (2011b) propose a full-waveform matching method with vertical-component data to retrieve focal mechanisms of microseismic events from shallow and deep borehole networks and apply the method to a petroleum field. In this study, we use 3C data to minimize uncertainties in the resolved focal mechanisms. We extend and adapt the full-waveform matching method of Li et al. (2011b) to derive focal mechanisms using 3C waveforms and additionally introduce the SV/P and SH/P amplitude ratios for dual-borehole arrays.

Using the known velocity structure, we first calculate the synthetic waveforms of all the possible focal mechanism solutions and then conduct a grid-search algorithm to evaluate the matching level between the observed and synthetic waveforms. To quantify the matching level, we develop a four-term objective function including P-wave first motions, P- and S-wave similarities, the SV/P amplitude ratio, and the SH/P amplitude ratio inspired by the Li et al. (2011b) study. The focal mechanism solution with the largest objective function is most likely to be the best. Before applying the solution to real data, we conduct a synthetic study below with a random location and small errors in velocity and attenuation to test the robustness and reliability of the method. The synthetic test proves that this method can sufficiently retrieve focal mechanisms with dual recording arrays. We then perform focal mechanism inversion using this method on carefully processed real data. We assume that the source mechanisms can be represented by double couples because the recorded waveforms present much stronger S-waves than P-waves, which cannot be explained by tensile opening (Pearson, 1981). Many studies note that microseismic events are mostly shear failure along preexisting fractures and are caused by elevated pore pressure (Warpinski, 1997, 2010; Terakawa, 2014).

We demonstrate that the retrieved focal-plane mechanisms can be used to map the stress field considering multiple events at a given region. A group of focal-plane mechanisms can determine the orientation and relative magnitude of the principal stress tensor (Angelier, 1979, 1984; Michael, 1987; Gephart, 1990). With the inverted stress pattern from focal mechanisms, we subsequently distinguish the fault plane from the auxiliary plane based on the Coulomb failure function (CFF) (Coulomb, 1773). Therefore, we produce the underlying fracture geometries independent of event locations contributing additional constraints for resolution of the stimulated fracture network. Furthermore, considering that the elevated pore fluid pressure triggers seismic slip on favorably and unfavorably

oriented preexisting faults, we estimate the minimum pore fluid pressure perturbation at each event location.

MICROSEISMIC DATA SET

The microseismic data set discussed here comes from the Barnett Shale. The Barnett Shale reservoir has extremely low matrix permeability in the range of microdarcies to nanodarcies (Johnston, 2004) and suggests some degree of natural fracture development (Gale et al., 2007; Bruner and Smosna, 2011). Multistage hydraulic fracturing in horizontal wells is used to enhance production. A microseismic survey of the five hydraulic fracturing stages is available for study. For each stage, the microseismic signals are recorded by the two monitoring arrays of 3C downhole geophones simultaneously. The hydraulic stimulation is carried out in five boreholes, but the microseismicity is recorded using only two arrays for each stage. One of the monitoring arrays has 12 3C geophones, whereas the other has eight 3C geophones. The geophones are deployed with spacing of approximately 15 m (approximately 50 ft). Even though we have microseismic data from all five injection stages, considering the geometry coverage, in this paper, we carried out focal mechanism inversion and data analysis only for stage 5 because the recording geometry for stage 5 can well constrain the inversion. A schematic diagram of the wells and geophone positions is shown in Figure 1a and 1b. Microseismic events were recorded by the arrays in observation wells labeled A (12 geophones) and B (eight geophones). The distances between microseismic events and recording arrays are typically less than 609 m (2000 ft), so that there is a relatively high signal-to-noise ratio (S/N). A total of approximately 1000 events were located using a migration-based mapping technique, which can mitigate picking errors in P- and S-arrival identification (Kao and Shan, 2004; Kuang et al., 2013; Zhang and Zhang, 2013). During hydraulic fracturing, microseismic events occur around the perforation shots with magnitudes typically ranging from -3 to -1 . The velocity model for location, as shown in Figure 2, was derived from the well-log data and was calibrated using perforation shots. Because our study region is within 609 m (2000 ft) and the provided formations are nearly horizontal, the assumption of a 1D velocity model is reasonable. An isotropic 1D velocity model is used here because we do not see significant S-wave splitting, which would indicate that the anisotropy is relatively small compared with the general uncertainties in velocity.

METHODOLOGY

Identification of clear P- and S-waves is essential in our focal mechanism inversion algorithm, which uses full-waveform matching. However, only some of the 1000 located events present strong P- and S-waves. Our first step is to manually select relatively strong microseismic events in which the P- and S-waves can be clearly identified based on the S/N. One typical strong event is shown in Figure 3. The 3C raw waveforms are plotted by concatenating all 20 sensors together in the H1 component (blue), H2 component (green), and vertical component (red). The S/N can be as large as 20 or more; thus, noise is not a concern. As denoted by the large blue dots in Figure 1, we select 47 strong events to subsequently conduct full-waveform focal mechanism inversion.

The source focal mechanism can be represented by a three-by-three second-order moment tensor with six independent components (Aki and Richards, 2002). In this study, we assume that the

focal mechanisms of microseismic events can be represented by pure double couples, although it is possible that a small volume change or compensated linear vector dipoles part may also exist (Warpinski et al., 2012; Song et al., 2014). In our inversion results, most events have large objective functions. But if the objective function is too low, we will remove those events for the following stress analysis. We describe the double-couple source in terms of strike, dip, and rake. The basic methodology is to match the observed P- and S-waves through elastic full-waveform modeling using the known velocity model and locations. After discretizing the source parameters (i.e., strike, dip, and rake), a grid-search algorithm is performed for each event. We simulate full waveforms for all possible pure double-couple focal mechanisms, and we search for the best match between the observed and modeled P- and S-waves. Our 3C seismogram calculation applies the elastic-wave modeling of a point earthquake source in a multilayered half-space using the Thompson-Haskell propagator matrix technique (Zhu and Rivera, 2002). A triangle source time function is used for forward modeling, the duration of which can be estimated from the spectra of the recorded seismograms (Bouchon, 1981). The source focal mechanism is discretized as follows: strike ranging from 5° to 355° with an interval of 10° , dip ranging from 4° to 89° with an interval of 5° , and rake ranging from -175° to 175° with an interval of 10° . The rake range from -175° to 175° is used in our algorithm, instead of -90° to 90° , which is used in Li et al. (2011b). This leads to a total of 23,328 ($36 \times 18 \times 36$) possible focal mechanisms for each microseismic event. For each possible source orientation, elastic full-waveform modeling is performed with attenuation included. To determine the best focal mechanism for each event, we impose an objective function that characterizes the match level between the observed and modeled waveforms as follows (Li et al., 2011b):

$$\begin{aligned} \text{obj} = & a1 * f_1(\text{pol}(\text{obs}), \text{pol}(\text{syn})) + a2 * f_2(\text{obs} \otimes \text{syn}) \\ & + a3 * f_3\left(\left(\text{rat}\left(\frac{\text{SV}_{\text{obs}}}{\text{P}_{\text{obs}}}\right), \text{rat}\left(\frac{\text{SV}_{\text{syn}}}{\text{P}_{\text{syn}}}\right)\right)\right) \\ & + a4 * f_4\left(\left(\text{rat}\left(\frac{\text{SH}_{\text{obs}}}{\text{P}_{\text{obs}}}\right), \text{rat}\left(\frac{\text{SH}_{\text{syn}}}{\text{P}_{\text{syn}}}\right)\right)\right), \end{aligned} \quad (1)$$

where f_1, f_2, f_3 , and f_4 are different general functions for each term; $a1, a2, a3$, and $a4$ are the weighting factors; obs is the observed data; syn is the synthetic data; pol is the polarity of the first motion; rat is the amplitude ratio between the S- and P-waves; SV is the SV-wave; SH is the SH-wave; and P is the P-wave.

The only difference between Li et al.'s (2011b) objective function and this proposed one is that they use only the SV/P amplitude ratios, whereas we use the SV/P and SH/P amplitude ratios to better constrain the focal mechanisms. Moreover, we use 3C data in the inversion, whereas they use only vertical component data. This objective function in equation 1 contains four terms: The first term evaluates the coherency between observed and modeled P-wave first motions. We manually determine the P-wave polarities for the recorded waveforms, whereas for modeled waveforms, we sum over the waveforms in a specified time window around the P-wave first arrival and check the sign of the summation. The second term is a crosscorrelation, which measures the waveform similarity between the normalized observed and modeled waveforms in specified time windows. We normalize the waveforms while calculating the cross-

correlation coefficient so that the maximum value of the crosscorrelation is equal to one when the modeled waveforms perfectly match the observed waveforms. With the dual-array recording geometry in the studied data set, the S/P amplitude ratio can also be used to constrain the focal mechanisms. Furthermore, we separate the S-wave into SV- and SH-waves because the SV and SH modes have different radiation patterns, which can provide sufficient information to better constrain the focal mechanisms (Sileny and Milev, 2008). Therefore, the third and fourth terms in the objective function measure the difference of the SV/P and SH/P ratios between the observed and modeled waveforms in specified time windows, respectively. We use the unnormalized waveforms to calculate the

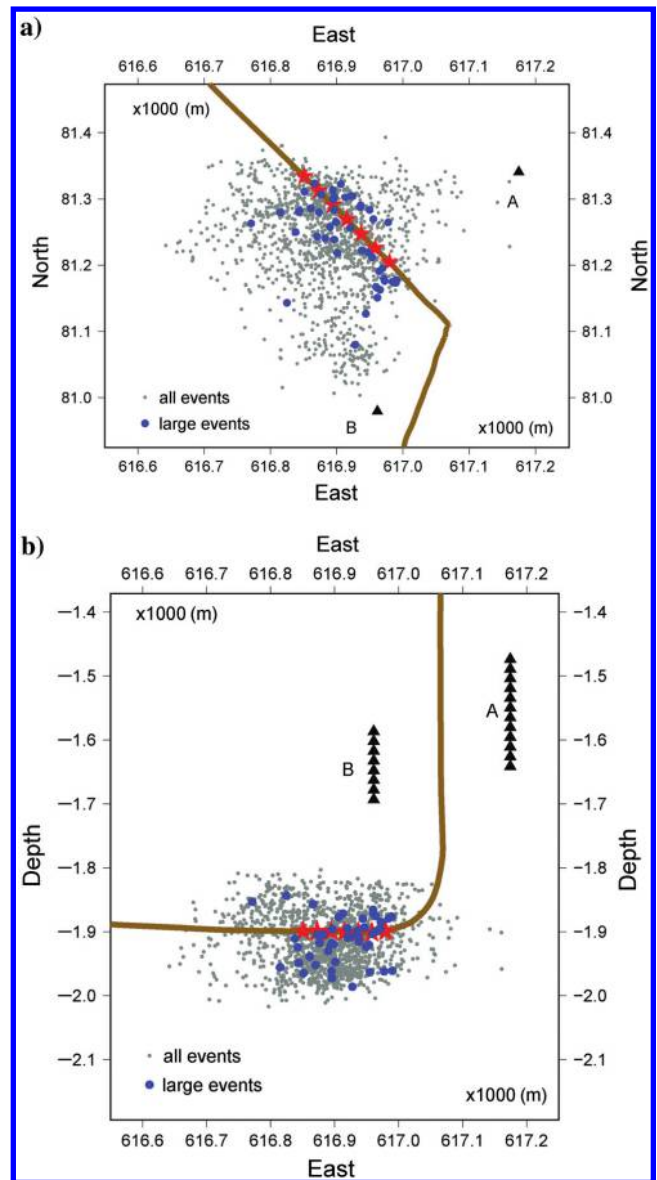


Figure 1. (a) Map view of the survey geometry including two recording arrays in wells A and B (black triangles), the treatment well (brown line), and perforation shots (red stars). Microseismic events (gray dots) cloud around the perforation shots. A total of 47 relatively large magnitude events are denoted using large blue dots. (b) Side view.

SV/P and SH/P amplitude ratios. The terms f_1 , f_2 , f_3 , and f_4 are the general functions that penalize the inconsistency if the term is not well-satisfied during waveform matching. To balance the contributions of these four terms, we set a_1 , a_2 , a_3 , and a_4 as weighting parameters. For each possible focal mechanism, after simulating the full waveforms, we compare the modeled waveforms with the observed waveforms and evaluate the objective function. When the modeled waveforms and the observed waveform are well-matched, the first and the second terms in the objective function will be maximized, but conversely, the third and the fourth terms will be minimized. To evaluate the four terms in one objective function, we set a_3 and a_4 as negative values. Thus, the best focal mechanism solution will have a maximized objective function; i.e., after compar-

ing the modeled and observed waveforms, the one with the highest objective function is taken as the best focal mechanism solution. Attenuation is included in our forward-modeling algorithm because it may affect the SV/P and SH/P ratios. In practice, we set reasonable uniform P and S attenuation factors for all layers. We set the Q_p factor as 30 and the Q_s factor as 50. With this value of Q_p and Q_s , we can best fit the observed data. We conducted a synthetic test considering the velocity error and attenuation error concurrently in the following section before applying this approach to field data.

SYNTHETIC TEST

We evaluate the accuracy and uncertainty of our inversion method through a synthetic test. We perturb the location, velocity, and attenuation from the reference parameters when we perform the inversion. In the synthetic test, we perturb the location 30 m from the reference location, considering that the location errors for this real data set are reduced when monitored using two wells. We shall describe the details for the synthetic test in the following.

To evaluate the eventual applicability of our field data set, we use the same station configuration illustrated in Figure 1. One strong event from this stage is selected to perform the synthetic test. After performing elastic forward-waveform modeling, the calculated 3C full waveforms for this event are treated as “real” data. We set the focal mechanism as follows: Strike is equal to 50° , dip is equal to 65° , and rake is equal to -50° . We use the reference P- and S-wave velocities (see Figure 2) to calculate the real data. The Q_p factor is set as 30, and the Q_s factor is set as 50 in the forward calculation.

Considering a real case, which usually includes location, velocity, and attenuation errors (Eisner et al., 2009), we perturb these input parameters when we apply our approach to invert focal mechanisms. To make the synthetic tests more realistic, we perturb the event location from the reference location and add an attenuation error up to 20% in the inversion. Furthermore, we use the P- and S-wave velocities, which are denoted using dashed lines in Figure 2, to account for velocity uncertainties. For real data processing, the velocity model is calibrated for each stage using perforation shots. Considering that we have already calibrated the velocity model using perforation shots, we perturb the velocity model in each layer with a maximum value of 4% by adding random velocity errors. Picking errors are not taken into account because we crosscorrelate the synthetic and observed waveforms; thus, no picking is needed. The weighting parameters are selected by trying different values. We use $a_1 = 20$, $a_2 = 10$, $a_3 = 5$, and $a_4 = 5$ for the synthetic test and real events. Through several synthetic tests, we find that the final solutions are not sensitive to small changes in the weighting parameters.

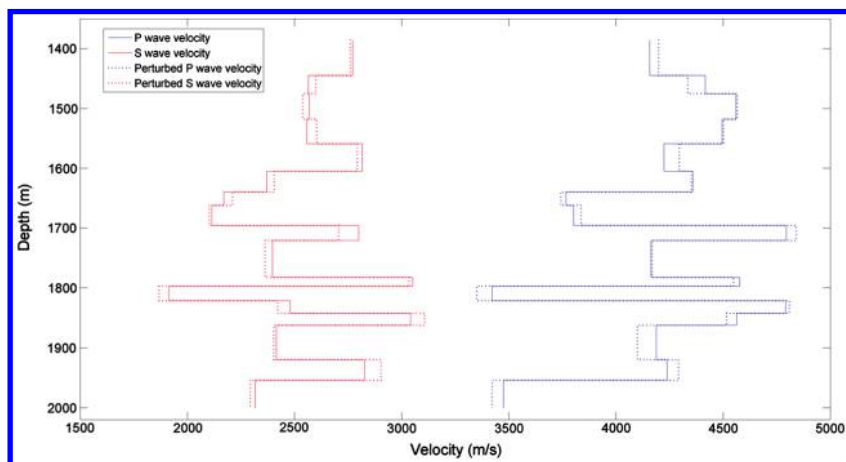


Figure 2. Layered velocity model for P- and S-waves in this region (solid lines). The velocity model is derived from nearby well logs and is calibrated using perforation shots. The dashed lines are randomly perturbed P- and S-wave velocities for the synthetic test.

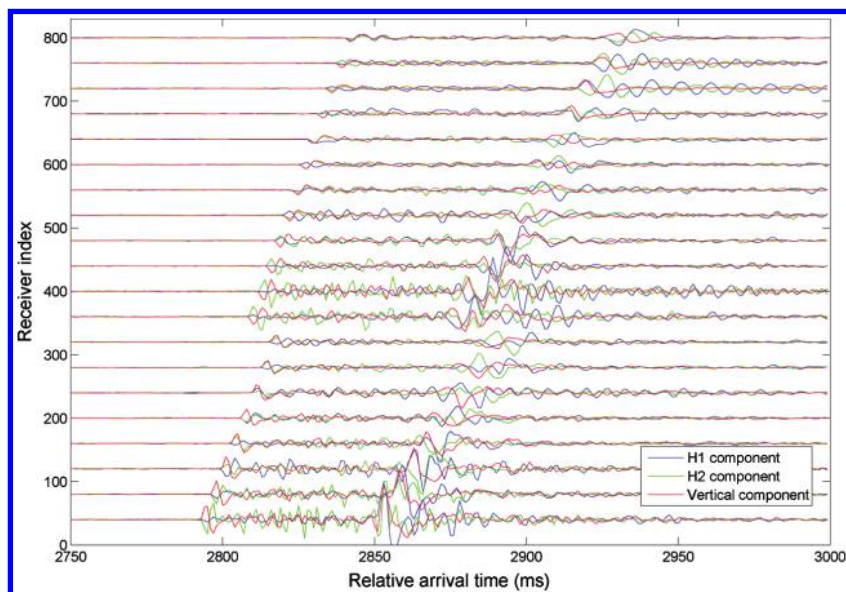


Figure 3. The 3C raw waveforms of one typical strong event. A total of 47 strong events such as this one are selected to perform focal mechanism inversion. The vertical component is plotted in red, and the two horizontal components are plotted in blue and green, respectively. High-S/N events are selected based on the magnitudes.

In the synthetic test, we perturb the event location 30 m from the reference location in the inversion. The 30 m of location error should be sufficient to account for the location uncertainties in this data set because the microseismic events are located using two bore-hole arrays with a migration-based locating technique, which can reduce the location uncertainties. After we apply our focal mechanism inversion approach for the first synthetic test, every 100th best search results for the best-fitting 1000 solutions are shown in Figure 4, ranked in order of their objective function values. The reference focal mechanism is shown in red. We can see that the objective function value decreases rapidly from approximately 30 to 13. Note that the corresponding focal mechanisms vary a lot for the best 1000 search results. It indicates that the focal mechanisms are well-constrained for the top search results. We show the 10 best solutions in Figure 5 and see that, within the best 10 solutions, the objective function value decreases only slightly from 30.65 to 29.41. However, the resolved focal mechanisms in Figure 5 indicate that the reference focal mechanism is reasonably well-resolved for all 10 best search results. Comparing Figure 5 with the best 1000 search results in Figure 4, we can conclude that, all of the first 10 best search results can be regarded as well-constrained solutions for this inversion problem with a relatively small degree of nonuniqueness. The ambiguities in strike, dip, and rake are within 10° and are caused by grid discretization and computational efficiency. We plot the distribution of objective function values for the 23,328 search results in Figure 6, again with the best solution ranking order. The objective function values decrease quickly from the first to the 1000th best solution, which indicates that the best solution is well-constrained.

Figure 7 shows the comparison between the observed (blue) and modeled (red) P- and S-waves. The P- and S-waves are windowed in the inversion using specified time windows based on the total duration of the P- and S-wave trains. For the P-waves, the transverse components are theoretically zero in the 1D velocity structure after we rotate the 3C waveforms into radial, transverse, and vertical components. That is why we have very weak transverse components in the P-wave comparison. The waveforms have been aligned by

removing time shifts, which are calculated through crosscorrelation between the observed and modeled waveforms. From the waveform comparison, we can see that the 3C waveforms are well-recovered for the P- and S-waves. Location and velocity errors mainly affect the arrival times. However, we crosscorrelate the observed data with the modeled data and align the waveforms in the inversion to eliminate the arrival-time effect. Attenuation error affects the amplitude of waveforms, as we can see from the S-wave comparison. However, the amplitude effect is relatively small so that a 20% attenuation error does not affect the SV/P and SH/P ratios significantly. This conclusion is also reached by Li et al. (2011a). Consequently, the inverted focal mechanism matches the reference focal mechanism well, even when attenuation error is present. Through the synthetic test with error added, the proposed waveform matching technique can produce robust and reliable focal mechanisms.

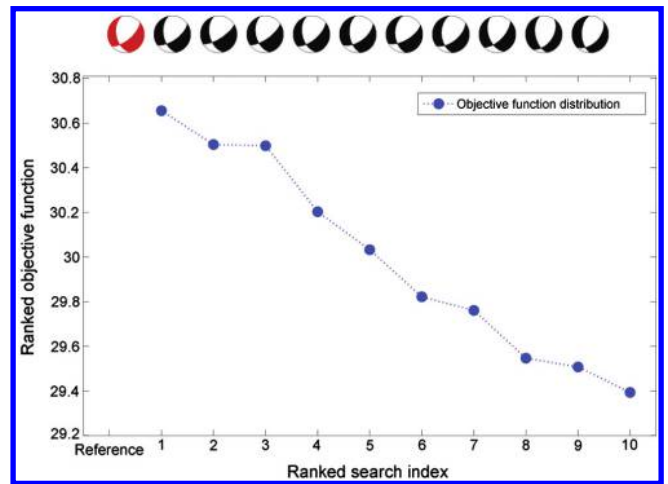


Figure 5. The distribution of the objective function for the first 10 best solutions after ranking, along with their corresponding focal mechanisms. The reference beach ball (red) is the one that is used to generate the reference data in the synthetic test.

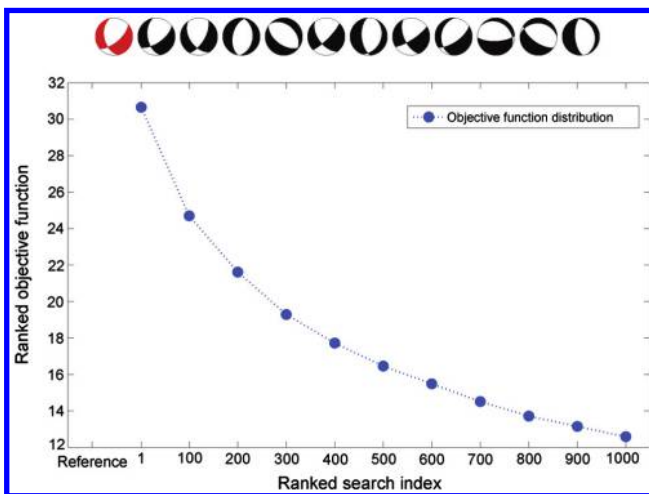


Figure 4. The distribution of the objective function for the first 1000 best solutions after ranking, along with their corresponding focal mechanisms for every 100th result. The reference beach ball (red) is the one that is used to generate the reference data in the synthetic test.

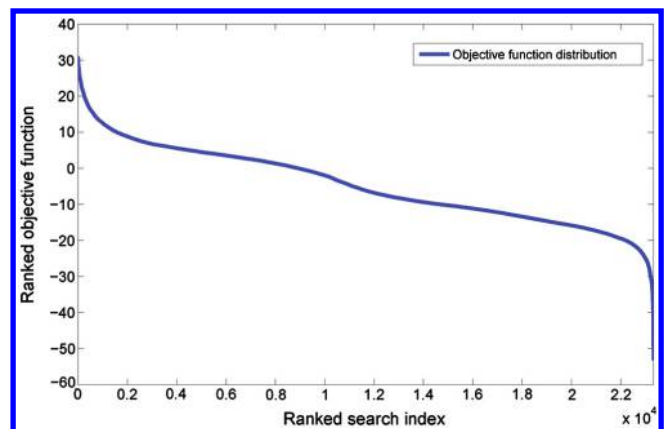


Figure 6. The distribution of the objective function for all 23,328 search results with the best solution order after ranking. The objective function values decrease quickly from the first to the 1000th best solution.

APPLICATION TO REAL DATA

Focal-plane mechanism results

We apply the technique outlined above to the 47 strong microseismic events. Before applying the focal mechanism inversion method to real data, we rotate the 3C raw waveforms into their radial, transverse, and vertical components based on the perforation shots. Figure 8 shows the rotated waveforms with respect to the raw waveforms in Figure 3. After rotation, we filter the 3C waveforms based on the time-variant spectrum analysis. The P-waves are filtered between 20 and 300 Hz. The S-waves are filtered between 10 and 150 Hz. The principal guideline of choosing a frequency band is to maintain the main energy of the P- and S-waves. In the inversion, we also filter the modeled waveforms using the same frequency band. The first motions of the P-waves are manually picked for the observed data. We pick only the positive/negative polarity. The P- and S-waves are windowed using appropriate time windows based on the total duration of the P- and S-wave trains. The P-wave window is 16 ms, and the S-wave window is 35 ms for this data set. The microseismic locations are determined using a migration-based locating method. These locations will be relocated in the version if the objective function is too low.

Figure 9 shows the final inverted focal mechanisms along with the located events (gray dots). Most of the events have normal faulting mechanisms, although there are also a few strike-slip faulting mechanisms. The dominance of normal faulting mechanisms suggests that the vertical stress is greater than the two horizontal principal stresses, but the occurrence of strike slip faulting mechanisms suggests that the vertical principal stress and maximum horizontal stress are approximately equal. Figure 10 shows a waveform comparison between the observed (blue) and modeled (red) data for the P- and S-waves from one event. The 3C waveforms between the observed and modeled data are well-matched. The objective function is well-satisfied even though the fits are not perfect, which could be caused by errors in velocity, location, attenuation, or the idealized approximation of the source time function. The presence of non-double-couple components (e.g., tensile components) of deformation may also contribute to misfit from the presumed double-couple solutions.

Stress inversion using focal-plane mechanisms

Using a family of earthquake focal-plane mechanisms to determine the stress field has been used successfully by many authors (Michael, 1984,

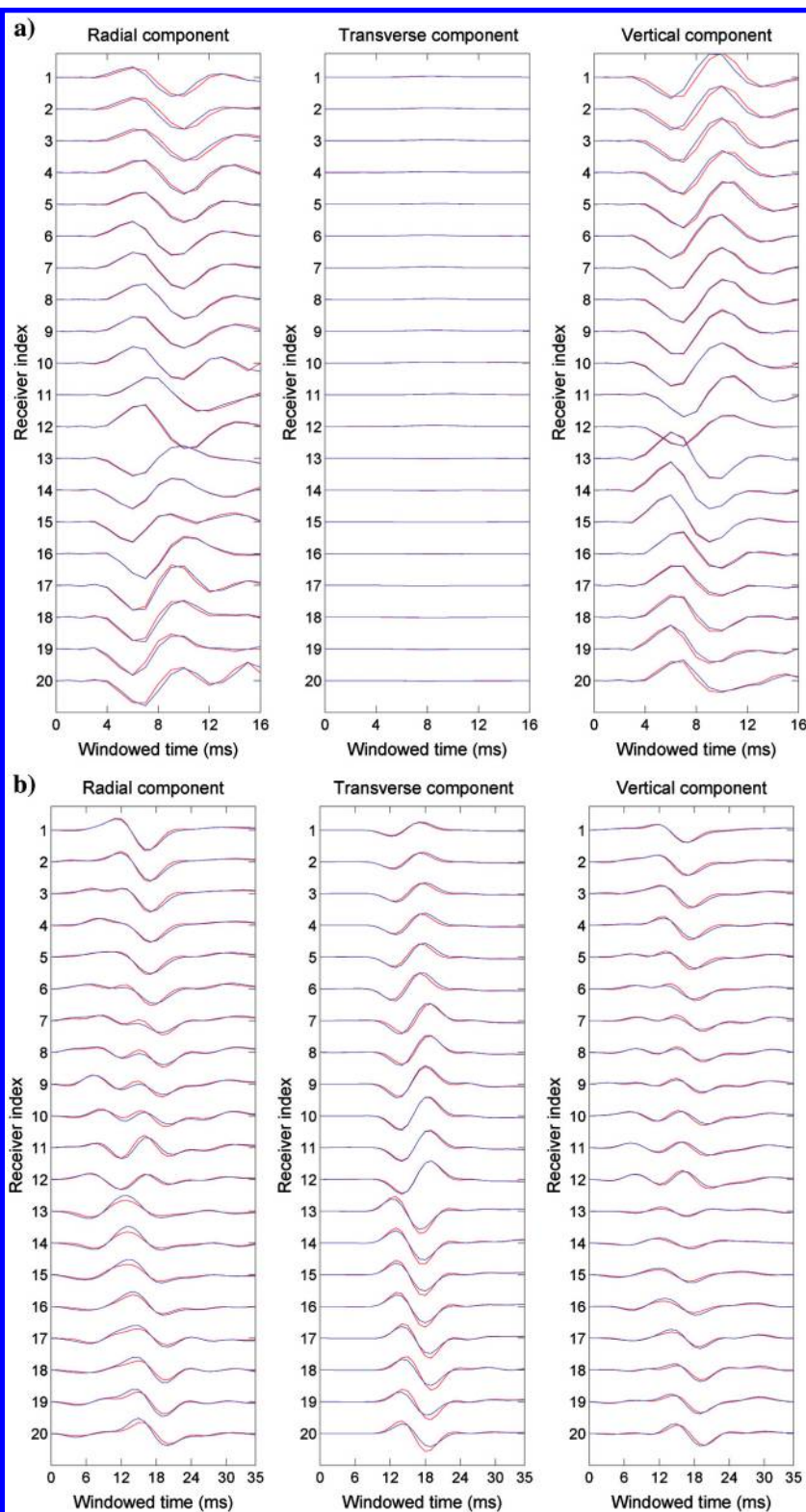


Figure 7. (a) P-wave comparison between real (blue) and modeled data (red). From left to the right are the radial components, transverse components, and vertical components. A preset P-wave time window is specified in the inversion. (b) S-wave comparison between real (blue) and modeled data (red). From left to right are the radial, transverse, and vertical components. A preset S-wave time window is specified in the inversion.

1987; Rivera and Cisternas, 1990; Terakawa et al., 2012). In standard methods of stress inversion, a uniform stress pattern, which includes three angles that define the orientation of the principal axes and the parameter $\Phi = (S_2 - S_3)/(S_1 - S_3)$ (Angelier, 1979) that defines the relative magnitude of S_2 , is estimated on the basis of the Wallace-Bott hypothesis that seismic slip occurs in the direction of the resolved shear traction on preexisting faults (Wallace, 1951; Bott, 1959). Here, S_1 , S_2 , and S_3 are the maximum, intermediate, and minimum compressive principal stresses, respectively. In this study, we adopt Michael's (1984, 1987) linear-inversion method by adding constraints on the magnitude of the tangential traction on the fault planes to stabilize the stress inversion. The inverted stress patterns are shown in Figure 11. The estimated directions of S_1 , S_2 , and S_3 are shown with red, blue, and green dots, respectively. The Φ value $((S_1 - S_3)/(S_2 - S_3))$ obtained from the inversions is approximately 0.8, indicating that $S_{H_{max}}$ is, on average, slightly less than S_V . The maximum principal stress S_V is nearly vertical. The intermediate and minimum principal stress axes are essentially horizontal, with directions of N60°E and S31°E, respectively. The horizontal stress directions inferred from the drilling-induced tensile fractures from a nearby vertical wellbore show that $S_{H_{max}}$ is oriented at N53°E. Thus, the inverted stress orientations prove that these focal mechanisms are well-determined with an acceptable degree of uncertainty.

To estimate absolute stress magnitudes, we follow the methodology outlined in Zoback (2007) and estimate the vertical stress from integration of rock densities from the surface to the depth of interest and the least principal stress from a leak-off test. Using these values and the value of ϕ derived from the inversions, we obtain absolute values of S_V , $S_{H_{max}}$, and $S_{h_{min}}$ at a depth of 1920 m, as 42, 40, and 30 MPa, respectively. The unperturbed pore pressure is estimated to be 20.5 MPa. This unperturbed pore pressure value comes from the engineers assuming that it is hydrostatic pressure. Using this information, we can determine which of the two possible planes represent the plane that slipped in the microseismic events and estimate the pore fluid pressure perturbation required to initiate slip on these small planes. We introduce the details in the following section.

FAULT-PLANE IDENTIFICATION AND PORE PRESSURE ESTIMATION

Fault-plane identification

In the hydraulic fracturing region, the injection of high-pressure fluid strongly increases the pore fluid pressure especially close to the induced hydraulic fractures. Compared with the highly elevated pore fluid pressure, the perturbation of the local stress field due to the opening of hydrofractures is quite smaller (Song et al., 2014). Based on the laboratory experiments of rock friction (Byerlee, 1978) and in situ stress measurements in deep wells and boreholes (Zoback and Healy, 1992; Zoback and Townend, 2001; Zoback, 2007), we assume a constant friction coefficient of 0.6. Microseismicity is attributed to

the increasing pore fluid pressure, which triggers shear failure on pre-existing fractures, many of which would not be likely to slip in the current stress field. We assume that microseismic events are governed by the Coulomb failure criterion and slip occurs in the direction of the resolved shear traction acting on the preexisting faults (Wallace, 1951; Bott, 1959). The CFF describes the proximity of fault to frictional sliding and is formulated as

$$CFF = \tau - \mu\sigma_n, \tag{2}$$

where τ and $\sigma_n = (S_n - P_p)$ are the resolved shear stress and effective normal stress on the plane of interest and μ is the friction coefficient.

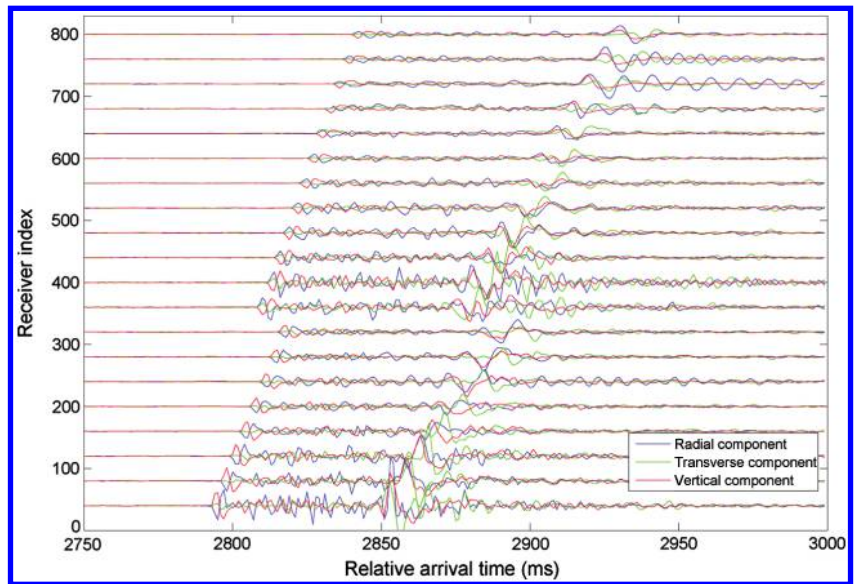


Figure 8. Rotated waveforms with respect to the raw waveforms shown in Figure 3. We rotate the 3C waveforms into the vertical, radial, and transverse directions. The vertical component is plotted in red, the radial component is plotted in blue, and the transverse is plotted in green.

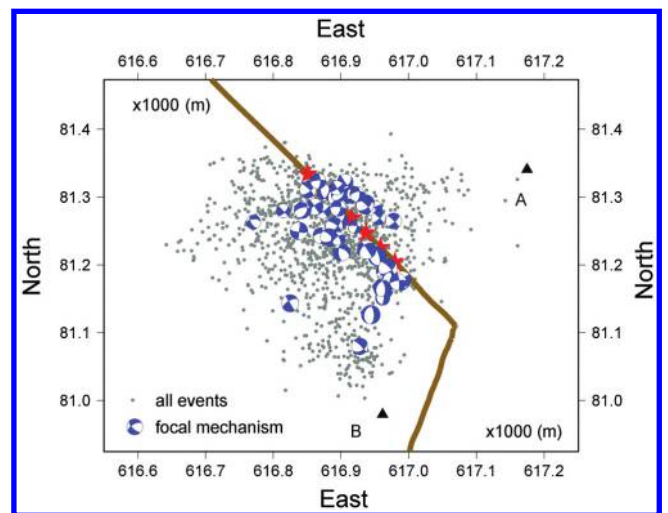


Figure 9. Inverted focal mechanisms for this stage, along with all located microseismic events. The magnitudes are denoted by the size of the beach balls.

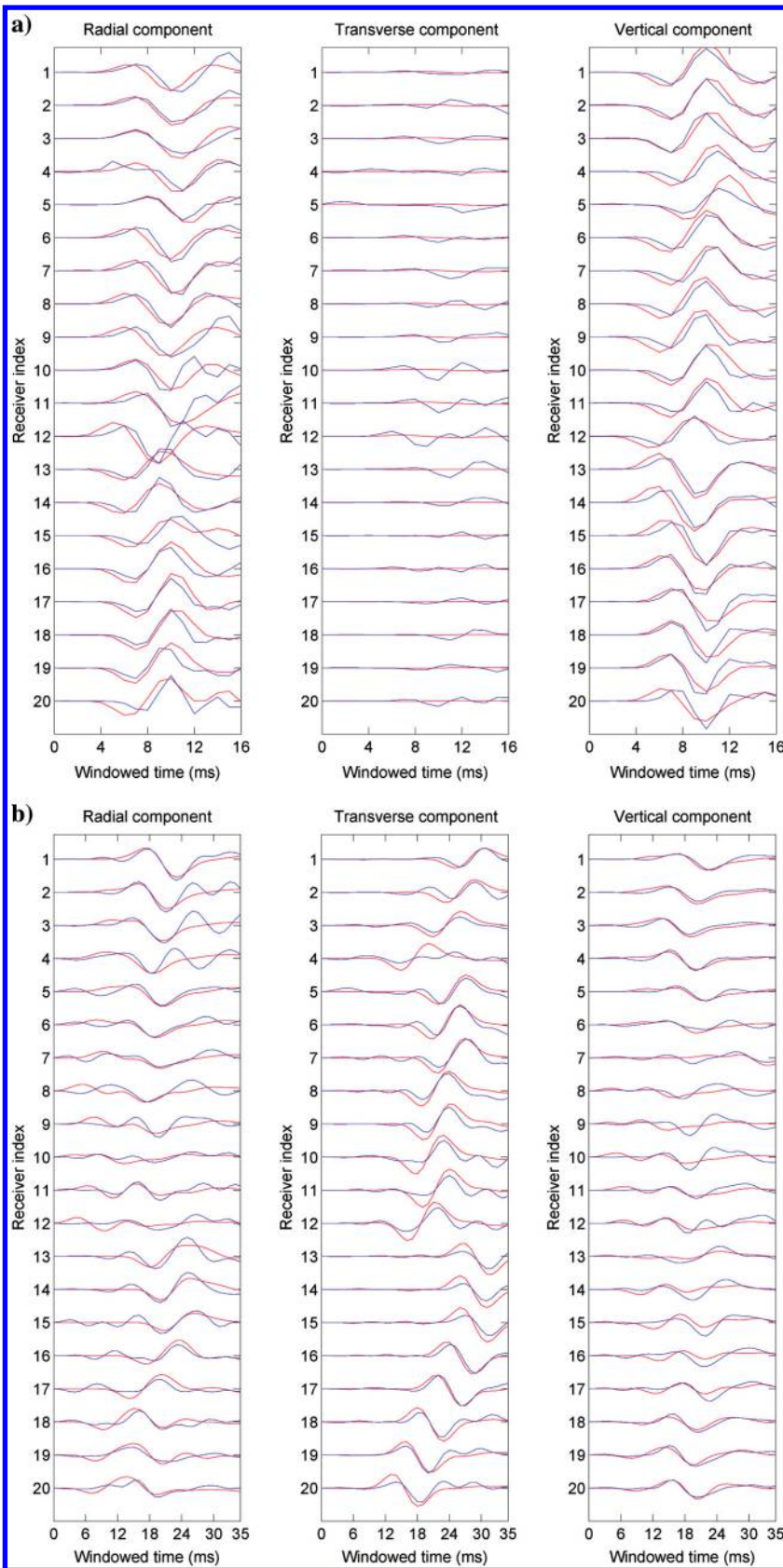


Figure 10. (a) The P-waves comparison between real (blue) and modeled data (red). From left to right are the radial, transverse, and vertical components. A preset P-wave time window is specified in the inversion. (b) S-wave comparison between real (blue) and modeled data (red). From left to right are the radial, transverse, and vertical components.

efficient. When the CFF is negative, a fault is stable because the shear stress is insufficient to overcome the resistance to sliding. However, as the CFF value approaches zero, frictional sliding occurs on a preexisting fault plane because there is sufficient shear stress to overcome the effective normal stress on the fault plane. With the increasing pore pressure, the effective normal stress decreases, which increases the CFF value. The basic idea of selecting the actual fault plane from the auxiliary plane can be illustrated using 3D Mohr diagrams. Each event has two possible fault planes; thus, there are totally $47 \times 2 = 94$ possible planes in Figure 12. For each nodal plane (i.e., each possible fault plane), we calculate the stress state on that plane and plot it in the 3D Mohr diagram. The plane with the higher CFF value (in units of MPa, in our case) is most likely to be the actual fault plane. Because the hydraulic fracturing process occurs over a few hours, we assume that poroelastic effects are minimal and that a change in pore pressure does not affect the absolute stress magnitudes. Using this method, we identify the fault planes of all inverted focal mechanisms, which are shown in Figure 12. As described below, the color of the point indicating a possible fault plane suggests that an increase in pore pressure is required to cause a fault slip. To give a statistic of all the focal planes (actual and auxiliary planes), we show the statistical fault orientations in Figure 13. These dots are also colored in CFF values, which share the same unperturbed pore pressure and other parameters with Figure 11. The planes with higher CFF values are selected to be the shearing planes. We can see that the shearing planes (red dots) are mostly steeply dipping with the dipping angle being approximately between 60° and 70° .

Pore fluid pressure estimation

During hydraulic fracturing, the pore pressure is elevated to a maximum value of approximately the least principal stress. Because the least principal stress is approximately 30 MPa and the initial pore pressure is approximately 20.5 MPa, the maximum pore pressure change is approximately 9.5 MPa. In actuality, the pore pressure can be slightly larger than the least principal stress right at the hydraulic fracture plane because pumping pressures exceed the least principal stress by an amount referred to as the net pressure. Thus, the maximum pore pressure change is approximately 10 MPa.

As shown in Figure 12, even though most of the identified faults have favorable orientations that allow slip to occur at pore pressure changes of a few MPa, there are some faults that are so poorly oriented that they require very high pore pressure perturbation to trigger the slip. Such

planes are likely to be stimulated only when they are close to the hydraulic fractures in which the pore pressure perturbation is maximum (we can also refer to Figure 14). As shown by the color of the points in Figure 12, knowing the stress state and the orientation of the likely fault plane, it is straightforward to estimate the pore pressure perturbation required to cause slip assuming a reasonable coefficient of friction. We go through all of the focal mechanisms and estimate the pore fluid pressure perturbation for the likely fault plane of each event.

Figure 14 shows the location and orientation of the likely fault planes associated with the focal mechanisms and estimated pore pressure perturbation. The size of the fault plane is estimated from the moment magnitude of the microseismic event based on standard seismological scaling factors (Stein and Wysession, 2003). However, to make the planes visible in the figure, we do not display them in even scales. A typical M-2 microseismic event represents slip on a plane approximately a meter in size.

DISCUSSION

In the inversion, due to the limited geometry coverage, the inverted source focal mechanisms are likely very poorly constrained and contain large errors. For some events that are far from the perforations, such as the event at the lower left corner in Figure 9, the recording geometry coverage is very poor. The inverted focal mechanism may have large uncertainties. In this case, we do two kinds of quality control analysis to decide whether we should keep or drop the inverted focal mechanism of some event. The first quality control is that we plot the top 20 searched focal mechanisms for that event. If the top 20 searched events are consistent, we consider the inverted focal mechanism of that event to be reasonable. Conversely, if the top 20 searched events vary too much, we will drop that event. The second quality control is that if the inverted focal-plane mechanism of one event requires extremely unreasonable pore pressure to slip, we will also consider that the event has very large uncertainty and drop it. Overall, for this data set, because there

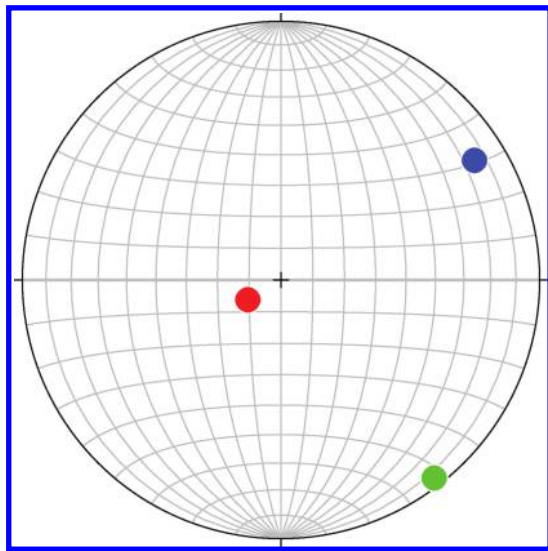


Figure 11. The stress pattern inverted from this stage. The red dot is the inverted direction of S1, the blue dot is the direction of S2, and the green dot is the direction of S3. Stress inversion retrieves three angles of the principal stresses and a parameter that gives the relative magnitude of S2, and $\Phi = 0.8109$.

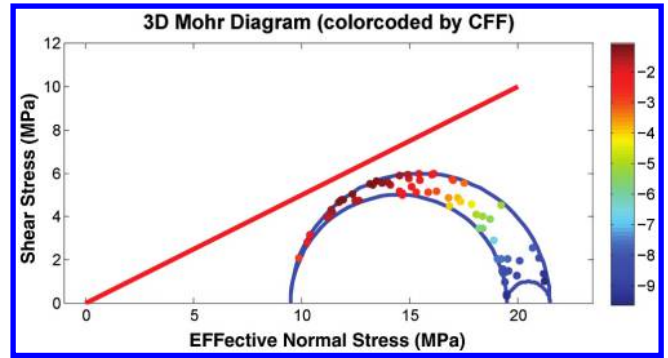


Figure 12. Focal mechanism planes plotted in a 3D Mohr diagram. The fault planes with higher CFF value are selected as actual planes. The selected fault planes are critically stressed in the current stress field, whereas the auxiliary planes are not critically stressed. Note, when it is the unperturbed pore pressure (red line), all the planes are stable. The CFF values are all negative.

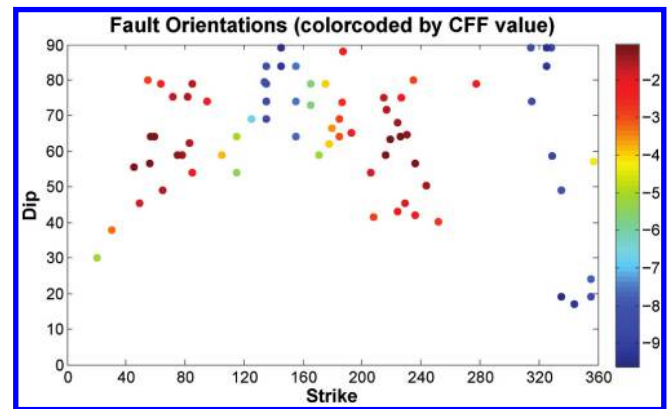


Figure 13. Fault orientation distribution for the inverted focal planes. The fault planes with higher CFF value are selected as actual planes, whereas the fault planes with smaller CFF value are auxiliary planes.

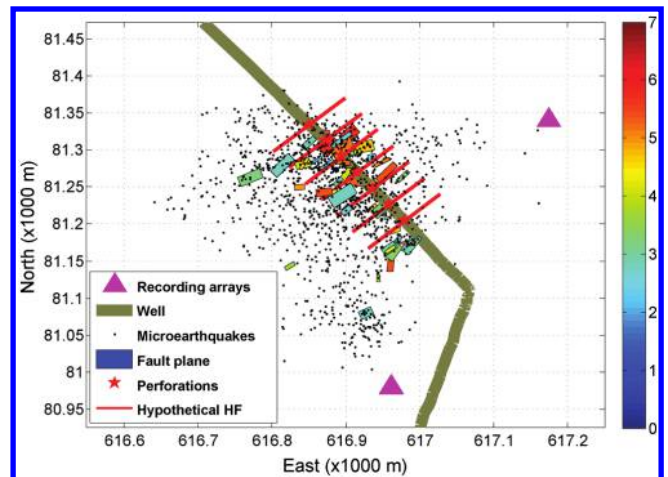


Figure 14. The distribution of the estimated minimum pore fluid pressure perturbation along with the orientations of the identified fault planes. The faults are colored in the pore pressure perturbation values in MPa. Perforation shots are plotted using red stars.

are only two recording wells, the uncertainties of the inverted focal mechanisms may be large due to the limited recording geometry, recorded data quality, and the simplified assumption of the media and source. But still, it allows us to make geomechanical analyses such as stress inversion because the errors are random. Figure 14 shows that the great majority of planes that were slipping in the microseismic events were associated with a pore pressure perturbation of a few MPa, although a few more poorly oriented planes had slipped as a result of larger pore pressure perturbations. Correspondingly, the great majority of planes are steeply dipping normal faults, striking parallel to maximum horizontal principal stress. The fault planes in Figure 14 provide a sense of the stimulated fracture and fault geometry in the hydraulic region based on the microseismic analysis. Combining the distribution of microseismic events with the orientations of the planes that slipped, we find that, a large-scale fault striking in the direction of $S_{H_{\max}}$ is seen (Figure 14).

CONCLUSION

In this study, we extend an adaptive focal mechanism inversion method using a waveform matching technique. This method uses P-wave first motion, P- and S-waves similarity, the SV/P amplitude ratio, and the SH/P amplitude ratio between the observed and modeled data to determine microseismic focal mechanisms, in which subsurface velocity information is available. The synthetic test proves that this method can retrieve focal mechanisms robustly, even with random errors included. We apply this method to determine 47 large-magnitude events from a borehole data set with dual arrays in the Barnett Shale. The inverted focal mechanisms suggest that this is a normal faulting/strike-slip faulting regime. Moreover, we use these focal-plane mechanisms to invert for the local stress field. The inverted source focal mechanisms are likely to be very poorly constrained and contain large errors. But still, it allows us to make geomechanical analyses such as stress inversion because the errors are random. The stress inversions for this stage show that S_1 is near vertical and corresponds to S_v ; it is just a little bit larger than S_2 ($S_{H_{\max}}$) and that S_2 and S_3 ($S_{h_{\min}}$) are nearly horizontal. The orientation of $S_{H_{\max}}$ is N60°E, consistent with the orientation of drilling-induced tensile fractures in nearby vertical wells. With some reasonable assumptions, we derive the orientation and magnitude of the three principal stresses. We use this knowledge to select the fault planes that slipped in the microseismic events and estimate the pore fluid pressure perturbation needed to make them slip. The results show that most of the identified fault planes are steeply dipping normal faults striking approximately N60°E, which is parallel with $S_{H_{\max}}$. By combining the fracture orientations and event locations, we infer that there is a large-scale fault crossing through these wells. This method provides valuable knowledge for understanding multistage hydraulic fracturing during horizontal drilling and oil/gas production.

ACKNOWLEDGMENTS

We thank Total for providing this data set to perform our study and B. Hughes for the software used in Figure 12. We also appreciate the financial support of the National Earthquake Reporting Research Program of China Earthquake Administration under grant no. 201408018, and we thank CNPC for supporting the Elastic Seismic Imaging Research Project.

REFERENCES

- Aki, K., and P. Richards, 2002, *Quantitative seismology*, 2nd ed.: University Science Books.
- Angelier, J., 1979, Determination of the mean principal directions of stresses for a given fault population: *Tectonophysics*, **56**, T17–T26, doi: [10.1016/0040-1951\(79\)90081-7](https://doi.org/10.1016/0040-1951(79)90081-7).
- Angelier, J., 1984, Tectonic analysis of fault slip data sets: *Journal of Geophysical Research*, **89**, 5835–5848, doi: [10.1029/JB089iB07p05835](https://doi.org/10.1029/JB089iB07p05835).
- Bott, M. H. P., 1959, The mechanics of oblique slip faulting: *Geological Magazine*, **96**, 109–117, doi: [10.1017/S0016756800059987](https://doi.org/10.1017/S0016756800059987).
- Bouchon, M., 1981, A simple method to calculate Green's functions for elastic layered media: *Bulletin of the Seismological Society of America*, **71**, 959–971.
- Bruner, K., and R. Smosna, 2011, A comparative study of the Mississippian Barnett Shale, Fort Worth Basin, and Devonian Marcellus Shale, Appalachian Basin: Technical Report DOE/NETL-2011/1478, National Energy Technology Laboratory (NETL) for The United States Department of Energy.
- Byerlee, J., 1978, Friction of rocks: *Pure Applied Geophysics*, **116**, 615–626, doi: [10.1007/BF00876528](https://doi.org/10.1007/BF00876528).
- Coulomb, C. A., 1773, Sur une application des regles de maximis et minimums a quelques problemes de statique, relatifs a l'architecture: *Memoires de Mathematique et de Physique, presentes a l'Academie. Royale des Sciences par drivers Savans, et lus dans ses Assemblees*, **7**, 343–382.
- Duncan, P., 2005, Is there a future for passive seismic: *First Break*, **23**, 111–115.
- Eisner, L., P. M. Duncan, W. M. Heigl, and W. R. Keller, 2009, Uncertainties in passive seismic monitoring: *The Leading Edge*, **28**, 648–655, doi: [10.1190/1.3148403](https://doi.org/10.1190/1.3148403).
- Gale, J. F. W., R. M. Reed, and J. Holder, 2007, Natural fractures in the Barnett Shale and their importance for hydraulic fracture treatments: *AAPG Bulletin*, **91**, 603–622, doi: [10.1306/11010606061](https://doi.org/10.1306/11010606061).
- Gephart, J. W., 1990, Stress and the direction of slip on fault planes: *Tectonics*, **9**, 845–858, doi: [10.1029/TC009i004p0845](https://doi.org/10.1029/TC009i004p0845).
- Guilhem, A., and D. S. Dreger, 2011, Rapid detection and characterization of large earthquakes using quasi-finite-source Green's functions in continuous moment tensor inversion: *Geophysical Research Letters*, **38**, L13318, doi: [10.1029/2011GL047550](https://doi.org/10.1029/2011GL047550).
- Johnston, D., 2004, Technological advances expand potential play: *Oil and Gas Journal*, **102**, 51–59.
- Kao, H., and S. J. Shan, 2004, The source-scanning algorithm: Mapping the distribution of seismic sources in time and space: *Geophysical Journal International*, **157**, 589–594, doi: [10.1111/gji.2004.157.issue-2](https://doi.org/10.1111/gji.2004.157.issue-2).
- Kuang, W., W. Zhang, and J. Zhang, 2013, Locating microseismic events using S-wave data only: 83rd Annual International Meeting, SEG, Expanded Abstracts, 2243–2247.
- Li, J., H. S. Kuleli, H. Zhang, and M. N. Toksoz, 2011a, Focal mechanism determination of induced microearthquakes in an oil field using full waveforms from shallow and deep seismic networks: *Geophysics*, **76**, no. 6, WC87–WC101, doi: [10.1190/GEO2011-0030.1](https://doi.org/10.1190/GEO2011-0030.1).
- Li, J., C. Li, A. M. Scott, D. Ted, K. Keith, and M. N. Toksoz, 2014, Microseismic joint location and anisotropic velocity inversion for hydraulic fracturing in a tight Bakken reservoir: *Geophysics*, **76**, no. 6, C111–C122, doi: [10.1190/geo2013-0345.1](https://doi.org/10.1190/geo2013-0345.1).
- Li, J., H. Zhang, H. S. Kuleli, and M. N. Toksoz, 2011b, Focal mechanism determination using high-frequency waveform matching and its application to small magnitude induced earthquakes: *Geophysical Journal International*, **184**, 1261–1274, doi: [10.1111/gji.2011.184](https://doi.org/10.1111/gji.2011.184).
- Michael, A., 1984, Determination of stress from slip data: Faults and folds: *Journal of Geophysical Research*, **89**, 11517–11526, doi: [10.1029/JB089iB13p11517](https://doi.org/10.1029/JB089iB13p11517).
- Michael, A., 1987, Use of focal mechanisms to determine stress: A control study: *Journal of Geophysical Research*, **92**, 357–368, doi: [10.1029/JB092iB01p00357](https://doi.org/10.1029/JB092iB01p00357).
- Pearson, C., 1981, The relationship between microseismicity and high pore pressures during hydraulic stimulation experiments in low permeability granitic rocks: *Journal of Geophysical Research: Solid Earth*, **86**, 7855–7864, doi: [10.1029/JB086iB09p07855](https://doi.org/10.1029/JB086iB09p07855).
- Rivera, L., and A. Cisternas, 1990, Stress tensor and fault plane solutions for a population of earthquakes: *Bulletin of the Seismological Society of America*, **80**, 600–614.
- Sileny, J., and A. Milev, 2008, Source mechanism of mining induced seismic events — Resolution of double couple and non double couple models: *Tectonophysics*, **456**, 3–15, doi: [10.1016/j.tecto.2006.09.021](https://doi.org/10.1016/j.tecto.2006.09.021).
- Song, F., N. R. Warpinski, and M. N. Toksoz, 2014, Full waveform based microseismic source mechanism studies in the Barnett Shale: Linking microseismicity to reservoir geomechanics: *Geophysics*, **79**, no. 2, KS13–KS30, doi: [10.1190/geo2013-0094.1](https://doi.org/10.1190/geo2013-0094.1).
- Staněk, F., L. Eisner, and T. Jan Moser, 2014, Stability of source mechanisms inverted from P-wave amplitude microseismic monitoring data

- acquired at the surface: *Geophysical Prospecting*, **62**, 475–490, doi: [10.1111/1365-2478.12107](https://doi.org/10.1111/1365-2478.12107).
- Stein, S., and M. Wysession, 2003, *An introduction to seismology: Earthquakes and earth structure*: Blackwell.
- Terakawa, T., 2014, Evolution of pore fluid pressures in a stimulated geothermal reservoir inferred from earthquake focal mechanisms: *Geophysical Research Letters*, **41**, 7468–7476, doi: [10.1002/2014GL061908](https://doi.org/10.1002/2014GL061908).
- Terakawa, T., S. A. Miller, and N. Deichmann, 2012, High fluid pressure and triggered earthquakes in the enhanced geothermal system in Basel, Switzerland: *Journal of Geophysical Research: Solid Earth*, **117**, 2156–2202, doi: [10.1029/2011JB008980](https://doi.org/10.1029/2011JB008980).
- Tsuruoka, H., H. Kawakatsu, and T. Urabe, 2009, GRiD MT (grid-based real-time determination of moment tensors) monitoring the long-period seismic wavefield: *Physics of Earth and Planetary Interiors*, **175**, 8–16, doi: [10.1016/j.pepi.2008.02.014](https://doi.org/10.1016/j.pepi.2008.02.014).
- Wallace, R. E., 1951, Geometry of shearing stress and relation of faulting: *The Journal of Geology*, **59**, 118–130, doi: [10.1086/625831](https://doi.org/10.1086/625831).
- Warpinski, N., 2009, Microseismic monitoring: Inside and out: *Journal of Petroleum Technology*, **61**, 80–85, doi: [10.2118/118537-JPT](https://doi.org/10.2118/118537-JPT).
- Warpinski, N., and J. Du, 2010, Source mechanism studies on microseismicity induced by hydraulic fracturing: Presented at the SPE Annual Technical Conference and Exhibition, SPE.
- Warpinski, N. R., P. T. Branagan, R. E. Peterson, J. E. Fix, J. E. Uhl, B. P. Engler, and R. Wilmer, 1997, Microseismic and deformation imaging of hydraulic fracture growth and geometry in the C sand interval, GRI/DOE M-Site Project: Presented at the SPE Annual Technical Conference and Exhibition, SPE, doi: [10.2118/38573-MS](https://doi.org/10.2118/38573-MS).
- Warpinski, N. R., M. J. Mayerhofer, A. C. Bridges, and J. Du, 2012, Hydraulic fracture geomechanics and microseismic source mechanisms: Presented at the SPE Annual Technical Conference and Exhibition, SPE.
- Witten, B., and J. Shragge, 2015, Extended wave-equation imaging conditions for passive seismic data: *Geophysics*, **80**, no. 6, WC61–WC72, doi: [10.1190/GEO2015-0046.1](https://doi.org/10.1190/GEO2015-0046.1).
- Zhang, J., H. Zhang, E. Cheng, Y. Zheng, W. Kuang, and X. Zhang, 2014, Real-time earthquake monitoring using a search engine method: *Nature Communications*, **5**, 5664, doi: [10.1038/ncomms6664](https://doi.org/10.1038/ncomms6664).
- Zhang, W., and J. Zhang, 2013, Microseismic migration by semblance-weighted stacking and interferometry: 83rd Annual International Meeting, SEG, Expanded Abstracts, 2045–2049.
- Zhu, L., and L. A. Rivera, 2002, A note on the dynamic and static displacements from a point source in multilayered media: *Geophysical Journal International*, **148**, 619–627, doi: [10.1046/j.1365-246X.2002.01610.x](https://doi.org/10.1046/j.1365-246X.2002.01610.x).
- Zoback, M. D., 2007, *Reservoir geomechanics*: Cambridge University Press.
- Zoback, M. D., and J. H. Healy, 1992, In situ stress measurements to 3.5 km depth in the Cajon pass scientific-research borehole: Implications for mechanics of crustal faulting: *Journal of Geophysical Research*, **97**, 5039–5057, doi: [10.1029/91JB02175](https://doi.org/10.1029/91JB02175).
- Zoback, M. D., and J. Townend, 2001, Implications of hydrostatic pore pressures and high crustal strength for the deformation of intraplate lithosphere: *Tectonophysics*, **336**, 19–30.